

Apparent anisotropy in inhomogeneous isotropic media

Fan-Chi Lin and Michael H. Ritzwoller

Center for Imaging the Earth's Interior, Department of Physics, University of Colorado at Boulder, Boulder, CO 80309-0390, USA.

E-mail: fan-chi.lin@colorado.edu

Accepted 2011 June 3. Received 2011 June 6; in original form 2010 December 6

SUMMARY

Surface waves propagating through a laterally inhomogeneous medium undergo wavefield complications such as multiple scattering, wave front healing, and backward scattering. Unless accounted for accurately, these effects will introduce a systematic isotropic bias in estimates of azimuthal anisotropy. We demonstrate with synthetic experiments that backward scattering near an observing station will introduce an apparent 360° periodicity into the azimuthal distribution of anisotropy near strong lateral variations in seismic wave speeds that increases with period. Because it violates reciprocity, this apparent 1ψ anisotropy, where ψ is the azimuthal angle, is non-physical for surface waves and is, therefore, a useful indicator of isotropic bias. Isotropic bias of the 2ψ (180° periodicity) component of azimuthal anisotropy, in contrast, is caused mainly by wave front healing, which results from the broad forward scattering part of the surface wave sensitivity kernel. To test these predictions, we apply geometrical ray theoretic (eikonal) tomography to teleseismic Rayleigh wave measurements across the Transportable Array component of USArray to measure the directional dependence of phase velocities between 30 and 80 s period. Eikonal tomography accounts for multiple scattering (ray bending) but not finite frequency effects such as wave front healing or backward scattering. At long periods (> 50 s), consistent with the predictions from the synthetic experiments, a significant 1ψ component of azimuthal anisotropy is observed near strong isotropic structural contrasts with fast directions that point in the direction of increasing phase speeds. The observed 2ψ component of azimuthal anisotropy is more weakly correlated with synthetic predictions of isotropic bias, probably because of the imprint of intrinsic structural anisotropy. The observation of a 1ψ component of azimuthal anisotropy is a clear indicator of isotropic bias in the inversion caused by unmodelled backward scattering and can dominate and mask the 2ψ signal. Observers are encouraged to estimate and report 1ψ anisotropy in their inversions for azimuthal anisotropy, to model finite frequency effects using methods that are tailored to the method of measurement, and to estimate 1ψ and 2ψ anisotropy simultaneously.

Key words: Surface waves and free oscillations; Seismic anisotropy; Seismic tomography; Wave scattering and diffraction.

1 INTRODUCTION

Surface waves provide valuable and in some cases unique information about the seismic velocity structure of the crust and uppermost mantle. Recent deployments of large-scale seismic arrays, such as the USArray Transportable Array in the United States (Fig. 1), present the potential to produce high resolution images of both isotropic (e.g. Yang *et al.* 2008; Moschetti *et al.* 2010b) and anisotropic structures (e.g. Moschetti *et al.* 2010a; Lin *et al.* 2011). Due to strong heterogeneity at shallow depths, however, wavefield complications such as multiple scattering or ray bending (e.g. Lin *et al.* 2009), wave front healing (e.g. Nolet & Dahlen 2000), and backward scattering (e.g. Snieder 1986) can significantly affect the accuracy of surface wave tomography. This is particularly

true for azimuthal anisotropy, which has a relatively weak second-order effect on observations, and may be subject to both random and systematic bias from the stronger isotropic heterogeneities.

Wavefield complexities, in general, are most important when the wavelength of a wave is comparable to or greater than the scale of heterogeneity. In this case, ray theory breaks down. Numerous theoretical and numerical studies (e.g. Wielandt 1993; Friederich *et al.* 2000; Bodin & Maupin 2008) have shown that the apparent phase velocity (sometimes referred to as dynamic phase velocity) inferred from phase traveltimes with ray theory can differ substantially from the structural phase velocity. Recent work by Bodin & Maupin (2008), in particular, demonstrates the potential bias that isotropic heterogeneities can impart to measurements of (apparent) azimuthal anisotropy. These authors showed that

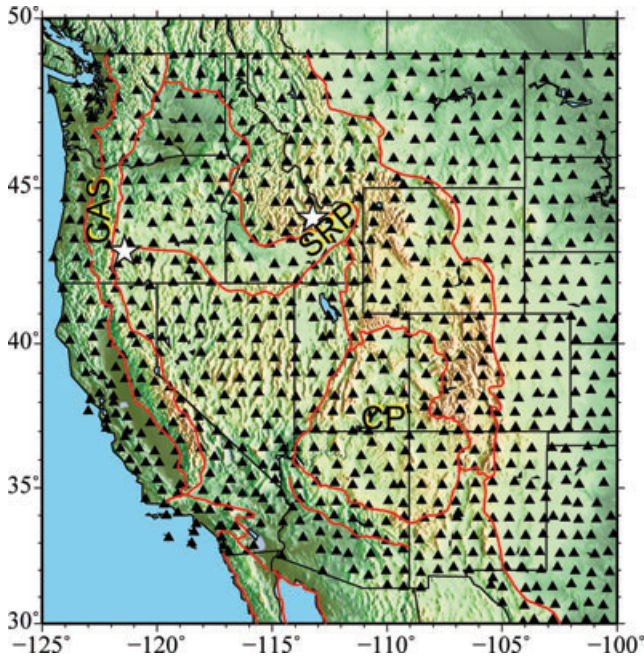


Figure 1. The USArray Transportable Array (TA) stations used in this study are identified by black triangles. The two stars identify locations used later in the paper. Red lines mark the tectonic boundaries in the western United States. CAS, Cascade Range; SNR, Snake River Plain; CP, Colorado Plateau.

azimuthal variations with a 360° , 180° and 90° periodicity (i.e. 1ψ , 2ψ , 4ψ components, where ψ is azimuth) can be introduced in the presence of an isotropic velocity anomaly due to effects such as reflection and wave front healing. We refer to such effects as ‘isotropic bias’, which produces an ‘apparent anisotropy’.

This study begins with simulations designed to estimate the effects of isotropic phase velocity anomalies on phase velocity measurements obtained with USArray data in the western United States. The simulations will be based on recently observed isotropic phase speed maps based on Helmholtz tomography (Lin & Ritzwoller 2011). Although any observed phase speed map is imperfect, we believe that the anomalies are approximately correct, particularly for the major structures across the region. Focus will be at periods of 40 s and above, where, as we will show here, isotropic bias is largest. The simulations are followed by applying a ray theoretic inversion to real data. The method applied is eikonal tomography (Lin *et al.* 2009), which we use here to obtain directionally dependent phase velocity measurements for Rayleigh waves between 30- and 80-s period across the western United States based on data from USArray (Fig. 1). The eikonal tomography method first tracks phase fronts across the entire array to determine the phase traveltimes for each earthquake and then estimates both the direction and phase velocity at each location based on the eikonal equation

$$\frac{\hat{k}_i(\mathbf{r})}{c'_i(\mathbf{r})} \cong \nabla \tau_i(\mathbf{r}), \quad (1)$$

where i is the earthquake index, \hat{k} is the unit wavenumber vector, τ is the phase traveltimes and c' is the apparent phase velocity. The eikonal equation is derived from the Helmholtz equation (e.g. Wielandt 1993)

$$\frac{1}{c_i(\mathbf{r})^2} = |\nabla \tau_i(\mathbf{r})|^2 - \frac{\nabla^2 A_i(\mathbf{r})}{A_i(\mathbf{r})\omega^2}, \quad (2)$$

where c is the structural phase velocity, A is the amplitude, and ω is

the angular frequency. The structural and apparent phase velocities are approximately equal ($c' \cong c$) when either the amplitude variation of the wave is small or frequency is high enough so that the amplitude-dependent term in eq. (2) can be neglected.

While the eikonal tomography method was developed for and was originally applied to ambient noise cross-correlation measurements (Bensen *et al.* 2007; Lin *et al.* 2008) by Lin *et al.* (2009), the method can be applied to earthquake measurements in a straightforward way (Lin *et al.* 2011). Here, we use data following more than 700 earthquakes. Segregating by propagation direction and averaging provides estimates of the azimuthal distribution of phase velocity for Rayleigh waves. Although these estimates are robust, we present evidence that they are biased by isotropic anomalies in a way that grows with period. Aspects of isotropic bias for ambient noise tomography are discussed by Ritzwoller *et al.* (2011).

In both the simulations and inversions with real data, we find that spurious 1ψ signals are particularly strong near the edges of strong velocity contrasts at long periods (>50 s). The observed 1ψ anisotropy pattern is, in fact, consistent with predictions from the simulations based on finite frequency kernels with strong backward scattering. Although body waves do have intrinsic 1ψ anisotropy that can affect surface wave measurements through mode coupling (Sieminski *et al.* 2007, 2009), this apparent 1ψ anisotropy of the inverted local surface wave phase velocity is non-physical (Chen & Tromp 2007), as it violates the principle of reciprocity. Thus, the observation of 1ψ anisotropy is a ‘smoking gun’ that presents clear evidence for isotropic bias in azimuthal anisotropy measurements. Although bias in the 2ψ component of anisotropy is harder to evaluate due to the presence of intrinsic anisotropy with this azimuthal periodicity, we present evidence for the existence of bias at long periods (>60 s) due to the effects of wave front healing. At periods below about 60 s, however, isotropic bias of 2ψ anisotropy is relatively weaker. Thus, Lin *et al.* (2011) combined earthquake and ambient noise dispersion measurements at periods below 54 s to model azimuthal anisotropy in the western United States. A study of how amplitude information can be used to reduce isotropic bias by applying the Helmholtz equation (eq. 2) directly is presented in a separate contribution (Lin & Ritzwoller 2011).

The outline of this paper is as follows. In Section 2, we present simulations to determine the probable patterns of 1ψ and 2ψ bias based on finite frequency kernels. In addition, we investigate whether biases arise from forward scattering effects that may potentially occur far from the observing station, such as wave front healing, or near-station effects such as backward scattering. In Section 3, we present the result of applying eikonal tomography to earthquake measurements across the western United States. In Section 4, we discuss the period dependence of both the 1ψ and 2ψ components of azimuthal anisotropy and also discuss the implications. In Section 5, we conclude with a discussion of the challenges that must be addressed in order to obtain reliable structural anisotropy information.

2 SIMULATION OF ISOTROPIC BIAS

To predict the effect of isotropic bias on measurements of surface wave azimuthal anisotropy that are interpreted ray-theoretically, we perform synthetic tests based on recent isotropic phase velocity maps observed across the western United States with the Helmholtz tomography method (e.g. Fig. 2a; Lin & Ritzwoller 2011). Different from ray theoretically based eikonal tomography, Helmholtz tomography, which estimates the local phase velocity by solving

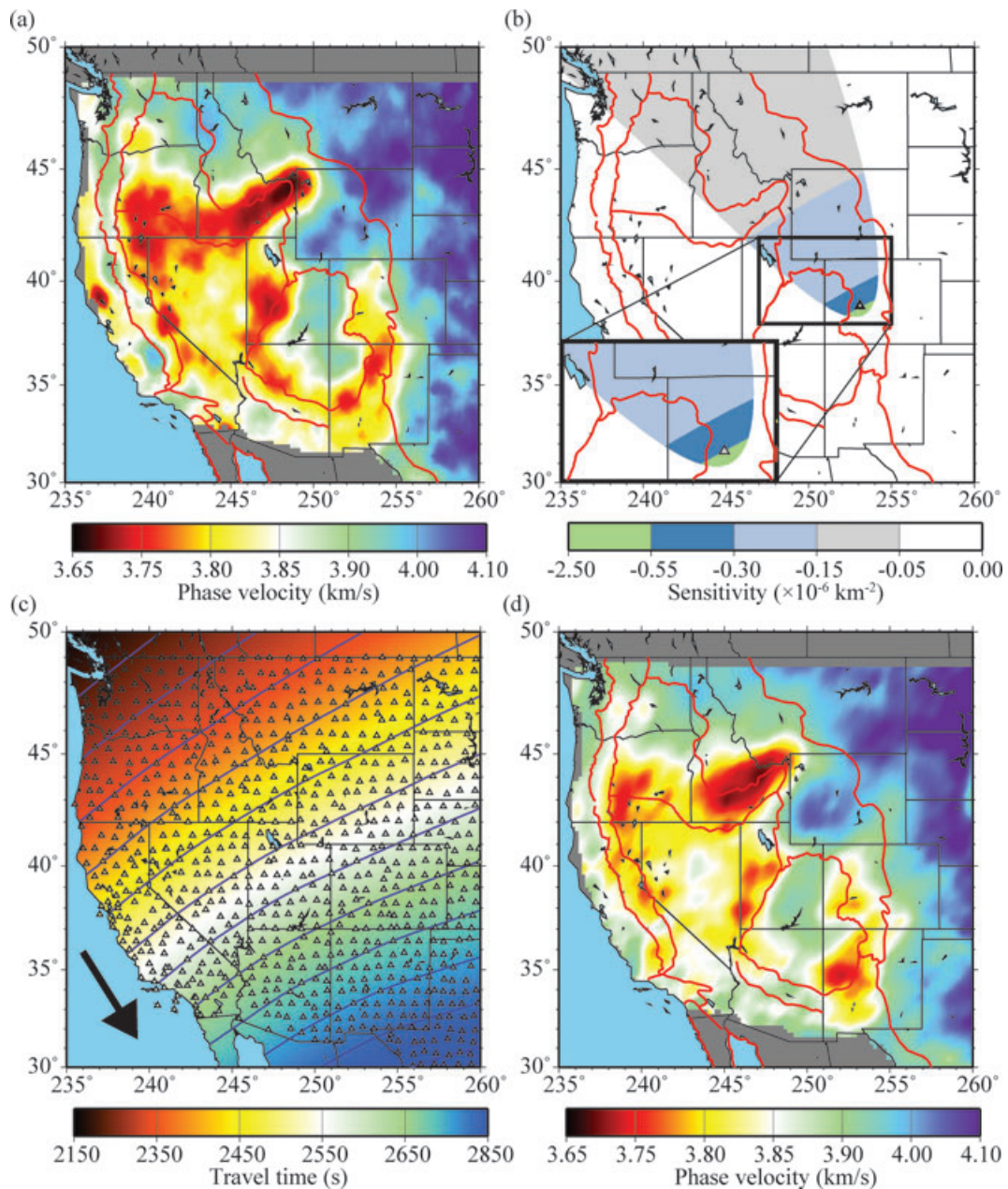


Figure 2. (a) The phase velocity map for the 60 s Rayleigh wave based on Helmholtz tomography (Lin & Ritzwoller 2011) used as the input model for the synthetic tests. (b) Example of the 60 s Rayleigh wave non-oscillatory, flat-topped finite frequency kernel used in the simulations. This kernel is for TA station Q22A (Crested Butte, Gunnison, CO) for an event in the northwest direction. The green area near the station defines the backward scattering region, which is separated from the broad region of forward scattering. The insert shows a blow up of the region near the station. (c) The 60 s Rayleigh wave phase traveltime map determined from the synthetic phase traveltime measurements across the array (triangles) for an event in the northwestern direction. Contours are separated by 60 s intervals. The arrow indicates the direction of wave propagation. (d) The apparent phase velocity derived from (c) based on the eikonal equation (eq. 1). The Snake River Plain low velocity anomaly shifts toward the northwest, opposite to the direction of wave propagation.

the Helmholtz equation (eq. 2), accounts for finite frequency effects and resolves the structural phase velocity more accurately. Simulated events at a distance of 90° from the centre of the observing array, each separated by 10° in azimuth, are used to synthesize phase traveltime measurements across the USArray stations (Fig 1). We adopt the non-oscillatory, flat-topped finite frequency kernels (e.g. Fig. 2b) similar to those described by Ritzwoller *et al.* (2002) to estimate traveltime perturbations due to structural perturbations within the region. For each event-station pair, the region with non-zero sensitivity (x) is defined by $|\Delta - (\Delta_1 + \Delta_2)| < 3c_0T_0/8$, where Δ ,

Δ_1 and Δ_2 are the distances between the event and receiver, the event and position x , and the receiver and x , respectively. c_0 is the reference phase speed (the average of the input model) and T_0 is the period. Where the kernel is non-zero, the sensitivity is constant for each cross-section perpendicular to the straight ray path and is set equal to $1/Rc_0$, where R is the width of the sensitivity zone for that cross-section. To avoid infinite values of the kernel, when $R < 20$ km we set it equal to 20 km.

Note that the kernel extends slightly beyond the station location in the direction of wave propagation. We refer to this as backward

scattering region in contrast to the rest of the kernel, which is the forward scattering region (Fig. 2b). The presence of backward scattering sensitivity is justified when backward scattering signals interfere with and are indistinguishable from the main arrival. Ritzwoller *et al.* (2002) truncated the sensitivity kernels to include only the forward scattering region, but we include the backward scattering part of the kernel here. This zone is very small; for example, if $c_0 T_0 \sim 240$ km, the backward scattering zone extends only ~ 45 km past the station. It may, therefore, be somewhat surprising that it makes such an important contribution to isotropic bias.

The non-oscillatory, flat-topped kernels used in our simulations are clearly an oversimplification of the complexity of the forward problem. In particular, the kernels do not depend on azimuth and focal mechanism, do not account for multiple scattering effects which can be important for wave front healing due to strong structural anomalies (Malcolm & Trampert 2011), and are probably too wide in the transverse direction (Yoshizawa & Kennett 2002; Zhou *et al.* 2005). The kernels make clear predictions about isotropic bias in azimuthal anisotropy, however, and their applicability is tested implicitly here as we compare the predictions with real observations in Section 3. Tests based on a direct numerical simulation (e.g. Fichtner *et al.* 2009; Tape *et al.* 2010) or other presumably more accurate kernels either with a more sophisticated theoretical treatment (e.g. Zhou *et al.* 2004), a numerical method (e.g. Tromp *et al.* 2005; Peter *et al.* 2007) or empirical sensitivity kernels (Lin & Ritzwoller 2010) is beyond the scope of this paper.

We follow the eikonal tomography method described by Lin *et al.* (2009) here to estimate the directionally dependent apparent phase velocities from the simulated data and in Section 3 based on real data. Eikonal tomography is a local inversion method (Pollitz & Snoke 2010), which directly determines the surface wave velocity structure by observing wave propagation across a dense array. Fig. 2(c) presents an example of the 60 s Rayleigh wave phase traveltime map determined from the synthetic phase traveltime measurements across the array from a single simulated event that lies northwest of the array. We apply a minimum curvature surface fitting method (Smith & Wessel 1990) to interpolate the inferred traveltimes onto a $0.2^\circ \times 0.2^\circ$ grid. The map is only meaningful where there are stations. The method smoothly extrapolates outside the region with station coverage, but the traveltimes are not constrained by the synthetic measurements. Based on eq. (1), the gradient of this phase traveltime map provides a direct estimate of the apparent phase speed, which is summarized in Fig. 2(d), as well as the direction of wave propagation at each location. The map is truncated to the region of the observing stations (Lin *et al.* 2009). The eikonal equation (eq. 1) naturally accounts for off-great-circle propagation but does not account for the finite frequency effects.

The phase velocity anomalies in Fig. 2(d) are shifted slightly toward the event direction relative to the input model (Fig. 2a). This is due to the non-zero backward scattering sensitivity for synthetic phase traveltime measurements at each station, which is not accounted for by the ray theoretically based inversion method. This is particularly clear for the low velocity anomaly associated with the Snake River Plain. In effect, the forward edge of sensitivity appears to lead the ray theoretic wave front. Thus, a finite frequency wave approaching a low velocity anomaly (e.g. the Snake River Plain in Fig. 2a) will sense the presence of the anomaly in front of the anomaly, which is not yet intersected by the ray. This forward sensitivity is actually caused by backscattering from a strong structural contrast. The effect will be to shift the anomaly in the direction of the incoming wave (Fig. 2d). As we will show in Section 3, this

same shifting phenomenon is also observed with real data. Waves that approach the anomaly from the opposite direction will experience the anomaly similarly, but will shift the apparent location of the anomaly in the opposite direction. Near the edges of velocity anomalies, therefore, the apparent speed of the wave will be azimuthally dependent, which imparts an apparent anisotropy to the measured phase speeds.

With multiple events, following the eikonal tomography method (Lin *et al.* 2009), phase speed measurements at the same location are averaged to estimate the isotropic phase speed structure where the uncertainty is also estimated based on the standard deviation of the mean. To determine the azimuthal variation, we estimate the directionally dependent phase speed and uncertainty based on the mean and standard deviation of the mean within each 20° azimuthal bin, respectively. To be consistent with the data processing for real observations, a 9-point (3×3 grid with 0.6° separation) averaging scheme is used to reduce small-scale variations (Lin *et al.* 2009) for directionally dependent measurements, which effectively also reduces the resolution to ~ 200 km (in contrast to ~ 70 km for isotropic maps). Fig. 3(a) shows an example from our simulations of this directional dependence in apparent phase speed measurements for the 60 s Rayleigh wave at a point near the Snake River Plain (star in Idaho in Fig. 1). A clear 1ψ component of apparent azimuthal anisotropy is observed which is about twice as strong as the apparent 2ψ component. Waves moving toward the southeast ($\sim 150^\circ$ from north), which is approximately perpendicular to the edge of the Snake River plain, appear to propagate slower than waves in the opposite direction. Both the apparent 1ψ and 2ψ signals are spurious, because the input model is isotropic. Because of the strength of the 1ψ signal, the traditional functional form for a weakly anisotropic medium (Smith & Dahlen 1973), which contains only even order sinusoids, is inappropriate to analyse azimuthal anisotropy. Instead, we will assume that phase velocity exhibits the following directional dependence

$$c(\psi) = c_{\text{iso}} \left\{ 1 + \frac{A_{1\text{psi}}}{2} \cos(\psi - \varphi_{1\text{psi}}) + \frac{A_{2\text{psi}}}{2} \cos[2(\psi - \varphi_{2\text{psi}})] \right\}, \quad (3)$$

where c_{iso} is the isotropic component of wave speed, ψ is the azimuthal angle measured positive clockwise from north, $A_{1\text{psi}}$ and $A_{2\text{psi}}$ are the peak-to-peak relative amplitude of 1ψ and 2ψ anisotropy, and $\varphi_{1\text{psi}}$ and $\varphi_{2\text{psi}}$ define the orientation of the anisotropic fast axes for the 1ψ and 2ψ components, respectively.

The best-fitting 1ψ and 2ψ components of anisotropy (e.g. Fig. 3a) across the entire western United States for the 60 s Rayleigh wave synthetic test are summarized in Figs 3(b)–(d) where the resulting isotropic phase speed map is also plotted in the background of Fig. 3(b). A clear correlation is observed between strong 1ψ anisotropic signals and regions with large structural contrasts, as Figs 3(b) and (c) show. The observed apparent fast directions always point toward higher velocities (Fig. 3b). In contrast, the 2ψ anisotropy is better correlated with linear features, such as the Snake River Plain, where either fast or slow directions align with the linear slow or fast anomaly, respectively (Fig. 3d). The isotropic map (Fig. 3b) is clearly much smoother than the input model (Fig. 2a) reflecting the discrepancy of the wide kernels and the ray inversion method used in our synthetic tests.

The apparent 1ψ and 2ψ anisotropy are both ‘isotropic bias’ of the estimates of azimuthal anisotropy because the input model is purely isotropic. To further understand the part of the sensitivity kernels that produce each kind of bias, we perform synthetic tests with kernels either with sensitivity to only forward scattering or

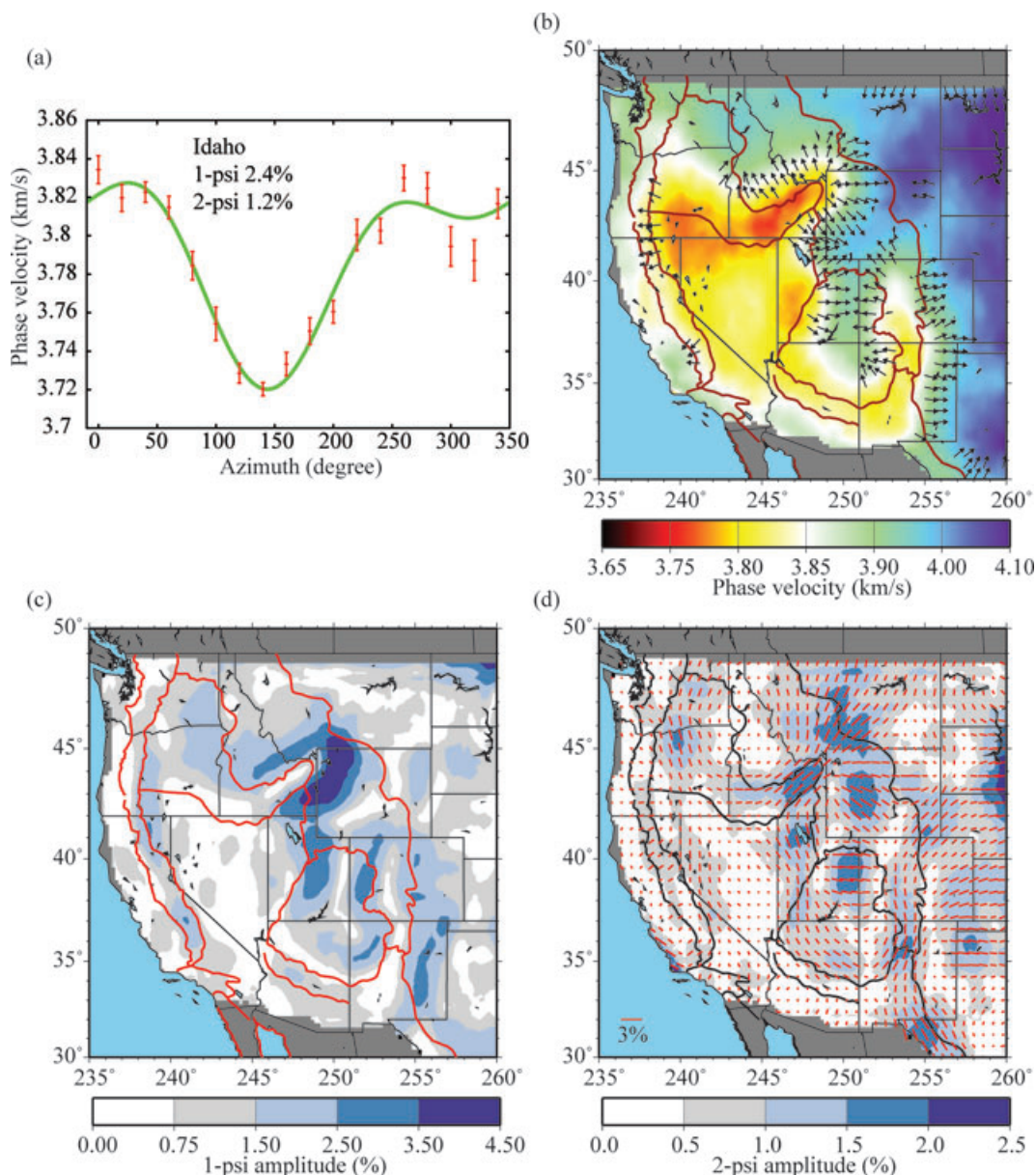


Figure 3. (a) The directionally dependent phase velocity measurements (red bars) for a point in Idaho northwest of the Snake River Plain (star in Fig. 1) for the 60 s Rayleigh wave simulation. The green line shows the best-fitting curve based on eq. (3) where the amplitudes of the 1ψ and 2ψ components are shown. (b) The predicted 1ψ fast directions at locations where the 1ψ amplitude is larger than 2 per cent are shown with arrows. The resulting isotropic phase velocity map is shown in the background. (c) The predicted 1ψ amplitudes. (d) The predicted 2ψ anisotropy. The fast propagation direction and anisotropy amplitude are presented by the orientation and length of the red bars. The anisotropy amplitude is also plotted in the background.

backward scattering (Fig. 2b). The observed 1ψ and 2ψ anisotropy from forward and backward scattering alone are summarized in Fig. 4. The forward scattering part of the kernel produces a weak 1ψ bias (Fig. 4a) but a strong 2ψ bias (Fig. 4b). Conversely, the backward scattering part of the kernel generates a strong 1ψ bias (Fig. 4c) and a weak 2ψ bias (Fig. 4d). Thus, as mentioned earlier, backward scattering controls the 1ψ bias. The 2ψ bias is caused by wave front healing, which is due to the broad forward scattering sensitivity. Note that the wave front healing effect can in general be a multiple scattering effect particularly if the structural anomaly is significant (Malcolm & Trampert 2011). Here, only the single scattering aspect of the effect is addressed based on our simulations.

3 OBSERVATIONAL METHODS AND RESULTS

Similar to Section 2, we follow the eikonal tomography method described by Lin *et al.* (2009) to determine the local directional dependence of phase velocities across the western United States with earthquakes measurements. Over 700 earthquakes that occurred between 2006 January 1 and 2010 April 11 with M_s magnitudes larger than 5.0 are used (Fig. 5). For each earthquake, we apply automated frequency-time analysis (FTAN) to measure phase traveltimes at each period for all available stations. Note that the FTAN method estimates the phase information (hence the phase traveltimes) at the time of the maximum amplitude of the group arrival for each

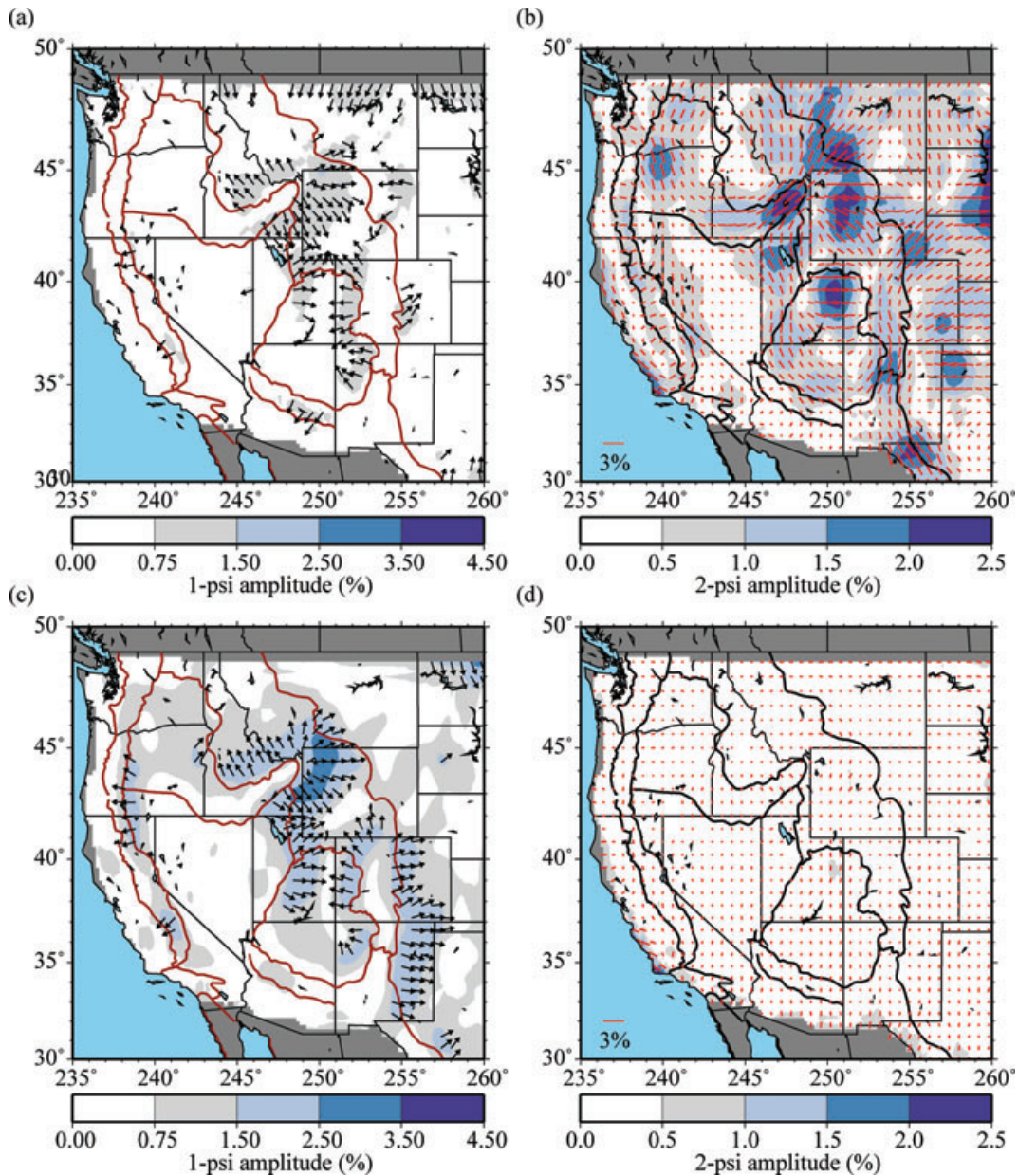


Figure 4. (a) and (b) The predicted 1ψ and 2ψ anisotropy based on the forward scattering kernels alone. In (a), the arrows present 1ψ fast directions with 1ψ anisotropy amplitude larger than 0.75 per cent. The anisotropy amplitude is plotted in the background. In (b), 2ψ fast propagation directions and anisotropy amplitudes are presented by the orientation and length of the red bars. The anisotropy amplitude is also plotted in the background. Panels (c) and (d) same as (a) and (b), but with backward scattering kernels alone. In (c), the fast directions are presented by arrays only when anisotropy amplitudes are larger than 1.5 per cent.

band-passed waveform. This means that scattered energy separated from the main arrival will not affect the phase traveltimes measurements. This is consistent with the use of non-oscillatory sensitivity kernels in the synthetic tests discussed in Section 2. We remove all measurements with signal-to-noise ratios less than 10. For each period, only earthquakes with valid measurements from at least 50 stations across the array are used for further analysis.

For each earthquake, we apply minimum curvature surface fitting to interpolate all phase traveltimes measurements onto a $0.2^\circ \times 0.2^\circ$ grid to construct the phase traveltimes maps for each period. The 2π phase ambiguity is corrected based on nearby stations and anomalous measurements are removed before a final map is constructed (Lin & Ritzwoller 2011). Figs 6(a) and (b) show two examples of

the resulting phase traveltimes maps for the 60 s Rayleigh wave propagating to the southeast and northwest, respectively. Similar to the simulation results presented in Section 2, the maps are only meaningful where there are stations. The apparent phase velocity maps computed from the gradient of the phase traveltimes using eq. (1) for each of these two earthquakes are presented in Figs 6(c) and (d). These maps are truncated to the region of the observing stations (Lin *et al.* 2009). Note that similar to the synthetic result shown in Fig. 2(d), for the earthquake in which the wave front propagates to the southeast, the apparent low phase speeds beneath the Snake River Plain shift toward the northwest (Fig. 6c). This implies that phase traveltimes measurements obtained on real data are also sensitive to downstream structures, presumably through

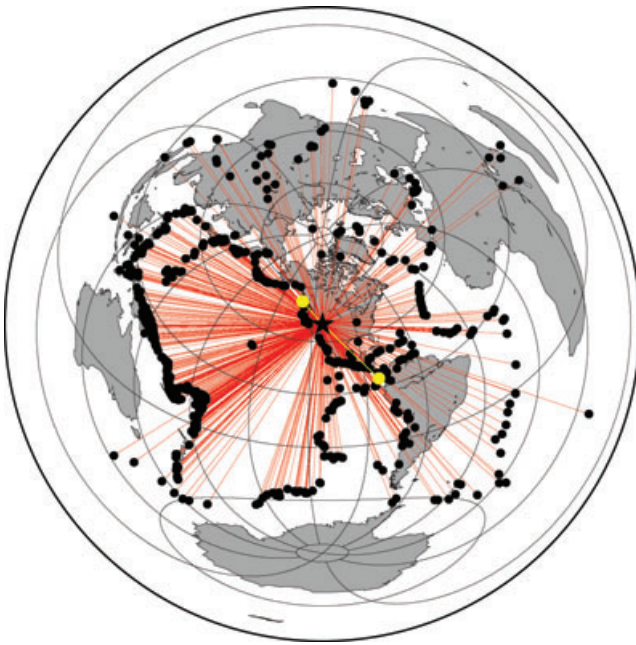


Figure 5. The earthquakes used in this study. Circles mark the location of the earthquakes, the star is the centre of our study region, and the lines between circles and the star are great-circle paths. The two yellow circles and paths mark the earthquakes used in Fig. 6.

backward scattering. A southeastern shift is less apparent for the wave propagating in the northwestern direction probably because of a cancellation between the slow anomaly of the Snake River Plain with the faster anomaly in southwest Wyoming (Fig. 6d).

As in Section 2, measurements from different earthquakes are statistically summarized to estimate both isotropic phase velocity and directionally dependent phase velocity and their uncertainties for each location. Figs 7(a) and (b) present two examples of the directionally dependent phase velocities for 60 s Rayleigh waves at locations near the Cascade Range and the Snake River Plain (stars in Fig. 1), respectively. Based on these observations, as well as those shown by Lin & Ritzwoller (2011), 1ψ and 2ψ are clearly the dominant and the only robust components of the observed azimuthal anisotropy, which justifies the use of eq. (3). For each location, we fit the observed velocity measurements with eq. (3) to simultaneously estimate the 1ψ and 2ψ components of azimuthal anisotropy. Significant 1ψ components of apparent anisotropy are observed at each location and both observations agree qualitatively with the synthetic predictions. The non-physical 1ψ apparent anisotropy signal (>3 per cent amplitude) dominates potential intrinsic 2ψ anisotropy, which typically have amplitudes less than 2 per cent (e.g. Marone & Romanowicz 2007; Lin *et al.* 2011).

The estimated 1ψ and 2ψ anisotropic signals and the resulting isotropic phase speed map from real data for 60 s Rayleigh waves across the western United States are summarized in Fig. 8. Clear correlations between strong 1ψ anisotropy and edges of structural boundaries are observed with fast directions that point toward the faster structures (Figs 8a and b). Regions with the most significant 1ψ anisotropy amplitudes (>4 per cent) are associated with the sharpest velocity contrasts in the western United States, such as the edges of the Snake River Plain slow anomaly, the Colorado Plateau fast anomaly and the fast anomaly of the subducted Juan de Fuca Plate near the Cascade Range. The pattern of the observed 1ψ anisotropy is similar to the synthetic prediction shown in Figs 3(b) and (c). The observed 2ψ anisotropy, on the other hand, is in general

weaker than the observed 1ψ anisotropy (1 per cent on average for 2ψ signals compared to 1.6 per cent for 1ψ signals) and shows a less clear relationship with the isotropic structures. This suggests that the observed 1ψ and 2ψ anisotropy are different in nature. The correlation between the observed (Fig. 8c) and predicted (Fig. 3d) 2ψ patterns is also weak (Section 4.1). This is probably due to the existence of intrinsic 2ψ anisotropy although inaccuracy of the forward scattering part of the sensitivity kernel may also contribute. The isotropic map (Fig. 8a) is clearly less smooth than the synthetic result (Fig. 3b) probably due to the wide kernels and the overly smoothed input model used in the synthetic test.

4 DISCUSSION

Simulations and observations with real data both establish that isotropic bias poses a significant problem for the inference of intrinsic azimuthal anisotropy and that this bias worsens as period increases. Thus, we consider here two principal questions. First, is there is a period threshold below which observers can safely ignore isotropic bias even within the context of ray theory (e.g. eikonal tomography)? Second, what can observers do to diagnose whether their estimates of azimuthal anisotropy are biased by isotropic heterogeneities and minimize isotropic bias?

As discussed above, finite frequency (non-ray theoretic) effects produce both 1ψ and 2ψ apparent anisotropy. However, the physics of the phenomena are different in each case. The apparent 1ψ signal is caused by backward scattering from a sharp velocity contrast in the neighbourhood of the observing station. The apparent 2ψ bias, on the other hand, is caused by wave front healing during the forward progress of the wave front, which is modelled by the broad forward scattering part of the finite frequency kernel. Because 1ψ anisotropy is non-physical for surface waves, its observation provides unambiguous evidence for isotropic bias. To draw conclusions about the period dependence of 1ψ isotropic bias, therefore, is straightforward and is the subject of Section 4.1. However, observations of 2ψ anisotropy may either be caused by bias from isotropic structures, by intrinsic anisotropy within the earth, or by an unknown combination of both. The period dependence of 2ψ isotropic bias, therefore, is more ambiguous, and is discussed in Section 4.2.

To investigate the period dependence of the isotropic bias, Figs 9 and 10 present the observed and simulated 1ψ and 2ψ anisotropy for the 40- and 80-s period Rayleigh waves to compare with the results at 60-s period in Figs 3 and 8. The input models for the 40 and 80 s simulations, which are the isotropic phase speed maps based on Helmholtz tomography (Lin & Ritzwoller 2011), are plotted in Fig. 11. In addition, to quantitatively compare the amplitude of the bias of anisotropy predicted from the synthetic tests to the observations with real data, Figs 12(a) and (b) present the percentage of the region with significant anisotropic amplitudes as a function of period. We consider anisotropic amplitudes of 2 and 1 per cent as the significance threshold for 1ψ and 2ψ anisotropy, respectively. The region east of 255° is not included in this analysis due to shorter spans of deployment for the stations in this region. To compare the direction of biased anisotropy predicted from the synthetic tests to observations with real data, Fig. 12(c) shows the vector correlation between the predicted and observed fast directions within the region of significant predicted and meaningful observed anisotropy amplitudes. Here, we define 2 and 1 per cent anisotropy amplitudes as significant for 1ψ and 2ψ predicted anisotropy, but 1 and 0.5 per cent as meaningful for 1ψ and 2ψ observed anisotropy, respectively. The vector correlation, ρ_{ab} , between two directional distributions

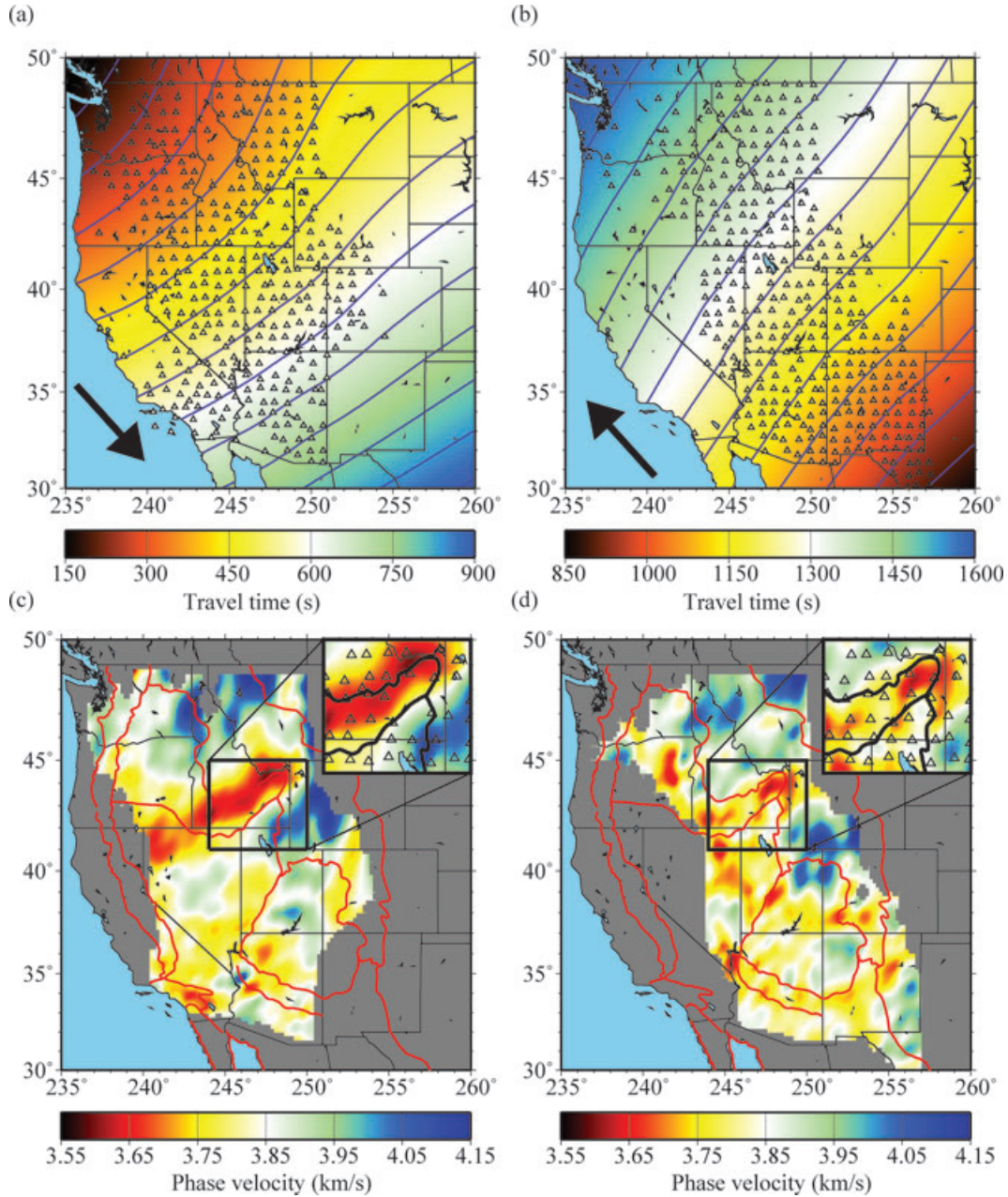


Figure 6. (a) The 60 s Rayleigh wave phase traveltime map for the 2008 January 9 earthquake near Queen Charlotte Islands ($M_s = 5.9$). The stations with available phase traveltime measurements used to construct the map are shown as triangles. Contours are separated by intervals of 60 s. The arrow indicates the direction of wave propagation. Panel (b) same as (a) but for the 2008 June 17 earthquake south of Panama ($M_s = 5.3$). (c) and (d) The apparent phase velocity maps derived from (a) and (b) based on eq. (1). The inserts show blow ups of the region near the Snake River Plain with the stations used shown as triangles.

\hat{a}_i and \hat{b}_i ($i = 1, \dots, N$) is defined as

$$\rho_{ab} = \frac{\sum_{i=1}^N (\hat{a}_i - \langle \hat{a} \rangle) \cdot (\hat{b}_i - \langle \hat{b} \rangle)}{\sqrt{\sum_{i=1}^N (\hat{a}_i - \langle \hat{a} \rangle)^2} \sqrt{\sum_{i=1}^N (\hat{b}_i - \langle \hat{b} \rangle)^2}}, \quad (4)$$

where \hat{a}_i and \hat{b}_i are unit vectors and i is the location index. Because of the 180° periodicity of fast directions for 2ψ signals, the azimuth of each fast direction is first multiplied by 2 for the 2ψ analysis before inserting into eq. (4). The correlation coefficient ρ ranges from -1 to 1 . When \hat{a}_i and \hat{b}_i point in the same direction for the 1ψ or 2ψ component the coefficient will equal 1 . The coefficient will be -1 when \hat{a}_i and \hat{b}_i point in the opposite direction everywhere for

the 1ψ component and are everywhere perpendicular to each other for the 2ψ case.

4.1 Period dependence of 1ψ isotropic bias

Due to the reciprocity principle, intrinsic surface wave structural anisotropy cannot manifest a 1ψ azimuthal component (Chen & Tromp 2007). The clear correlation between the observed 1ψ anisotropy and isotropic structural boundaries, therefore, suggests that the 1ψ anisotropy is purely isotropic bias. Note that while station timing errors can also cause spurious regional 1ψ anisotropy, this is clearly not the case here. The fact that the amplitude of the observed 1ψ anisotropy increases with period (e.g. Fig. 12a)

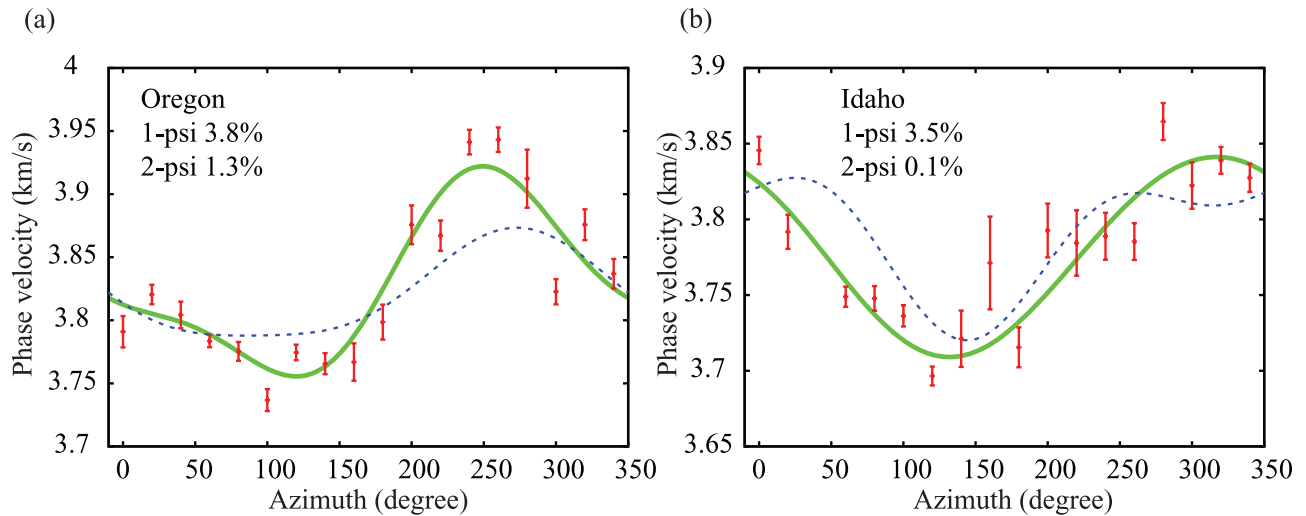


Figure 7. (a) The directionally dependent phase velocity measurements at a point near the Cascade Range (star in Fig. 1). The red bar summarizes all measurements within each 20° azimuthal bin with their mean and standard deviation of the mean. The green solid line shows the best-fitting curve of eq. (3) to the measurements with 1ψ and 2ψ amplitude also indicated in the panel. The best-fitting curve based on the synthetic test is also plotted as the blue dashed line. (b) Same as (a) but for a point near the Snake River Plain (star in Fig. 1)

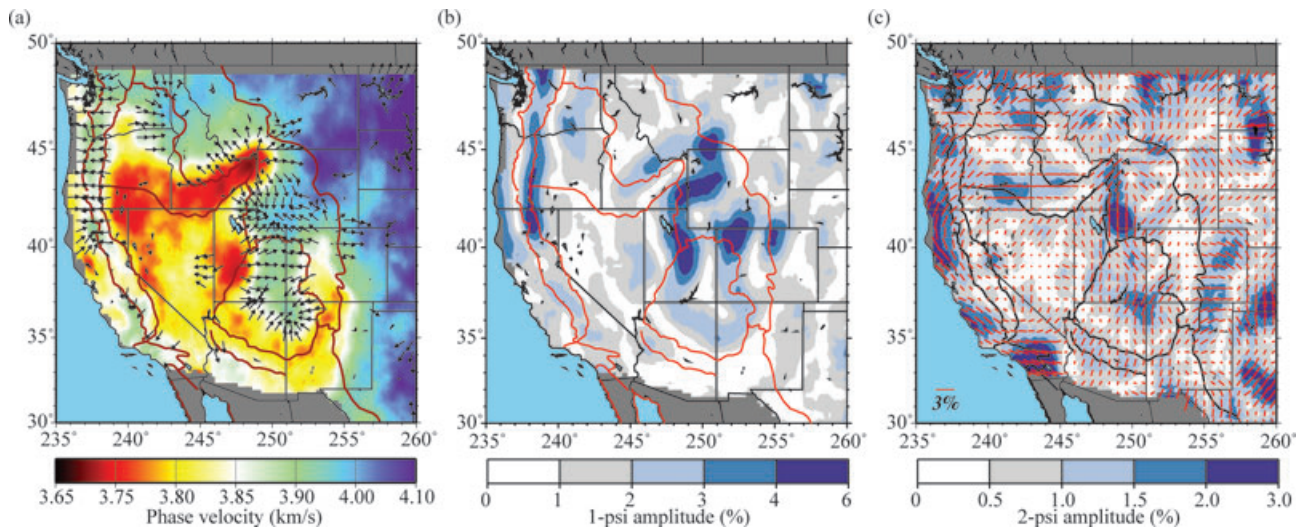


Figure 8. Same as Figs 3(b)–(d), but with real data measurements for the 60-s period Rayleigh wave.

indicates that it is a finite frequency effect. However, at what period does the 1ψ anisotropy become significant?

To compare with the observed results for the 60 s Rayleigh wave (Fig. 8), Figs 9(a), (b), (d) and (e) presents the observed 1ψ anisotropy at 40 and 80 s period, respectively. Measurable 1ψ signals are observed at both periods near the edges of prominent velocity anomalies, but the signals are significantly weaker at 40 s than at 60- or 80-s period. At 40-s period, the wavelength of the Rayleigh wave is ~ 150 km and the backward scattering sensitivity extends only ~ 30 km behind the station. Given the ~ 70 km station spacing for the USArray, a sharp structural boundary half way between two stations will have only a weak effect on the phase traveltimes at the two stations at this period. For periods shorter than 40 s, therefore, backward scattering is less severe than at longer periods for our station configuration. At 80-s period, the observed 1ψ anisotropy pattern (Fig. 9e) is similar to the 60-s result (Fig. 8b), although the pattern is more variable. This may be due to the degrading data quality at the longer periods (only 545

events satisfy the selection criterion at 80 s compared to 775 and 743 events for 40- and 60-s period, respectively).

The simulations for the 40- and 80-s period Rayleigh waves are summarized for apparent 1ψ anisotropy in Figs 10(a), (b), (d) and (e) to contrast with the observed results in Fig. 9 and the simulations at 60-s period presented in Fig. 3. Similar to the 60-s results, the predicted 1ψ anisotropy patterns correlate well with the observations based on real measurements, particularly at 80-s period. Again, the isotropic map (Figs 10a and d) is smoother than the real observation (Figs 9a and d) probably reflecting the wide kernels and the overly smoothed input models used in the simulations.

Fig. 12(a), which presents the percentage of the region with significant anisotropic amplitudes as a function of period, demonstrates that the synthetic tests slightly underestimate the real 1ψ isotropic bias, but does correctly predict the growth of the 1ψ signal with period. The discrepancy may be caused by random noise in the measurements, the sensitivity kernels inaccurately reflecting the real sensitivity of the measurements, or the underestimation of the

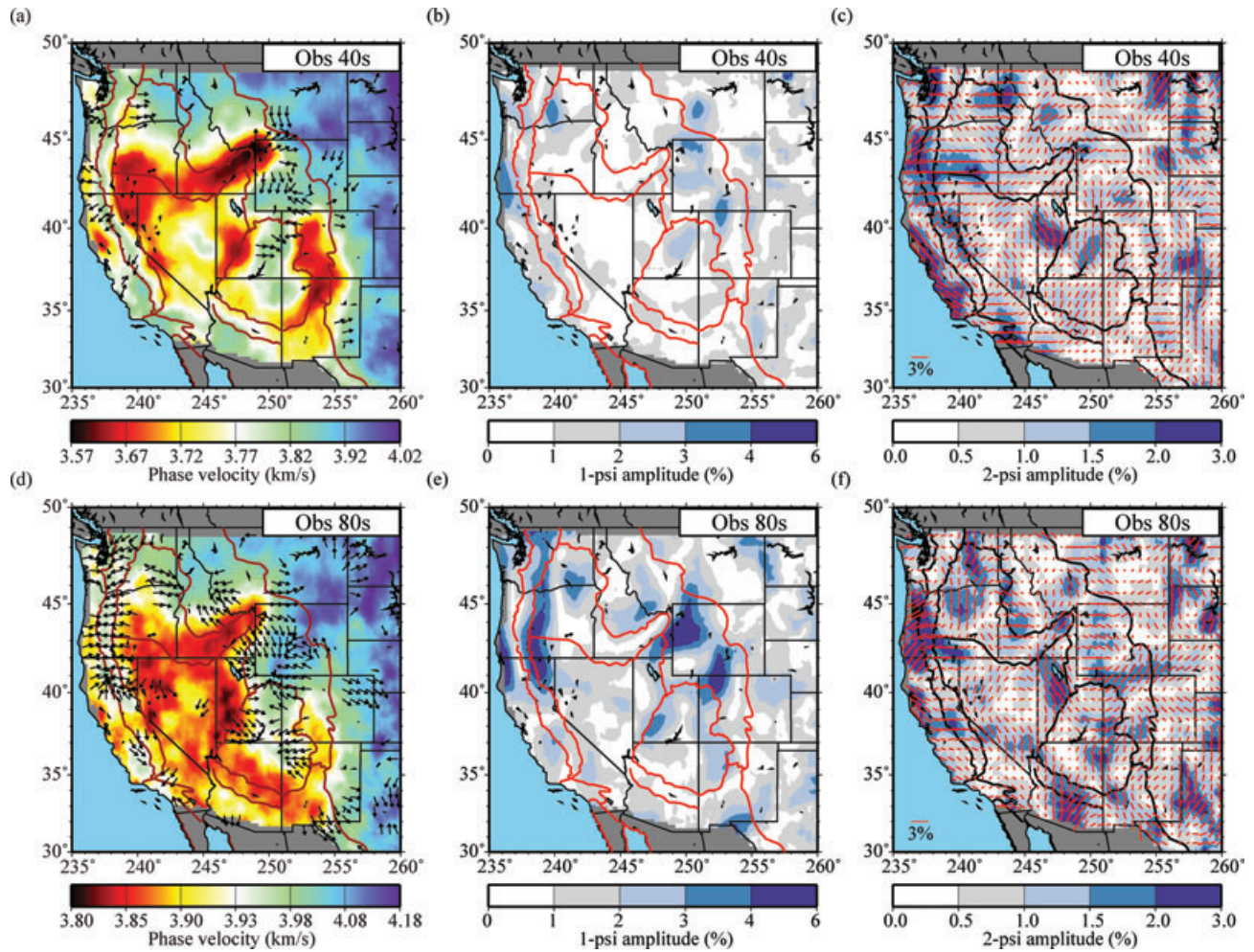


Figure 9. Same as Fig. 8, but with real data measurements for the 40 s (a)–(c) and 80 s (d)–(f) period Rayleigh waves.

amplitude of the isotropic velocity anomalies in the input phase velocity maps. Fig. 12 demonstrates that there is good correlation ($\rho > 0.7$) between the predicted and observed fast directions for 1ψ anisotropy at all periods, which suggests that the kernels we use to model backward scattering accurately reflect the observed bias in the 1ψ anisotropy.

In summary, the simulations and observations with real data agree substantively qualitatively and quantitatively. They establish that the 1ψ bias increases with period and becomes particularly significant above about 50-s period which the corresponding backward scattering sensitivity extended ~ 35 km behind each station roughly the same as the half station spacing for the USArray. For different station configurations, the period, which the 1ψ becomes significant will probably be different and be controlled by the station spacing and the resolution desired.

4.2 Period dependence of 2ψ isotropic bias

Because of the existence of intrinsic 2ψ anisotropy in the earth, determination of the bias in the 2ψ signal is much harder than for 1ψ anisotropy. At all periods, the observed 2ψ signal is some combination of real anisotropy and bias and separating these effects is problematic. This is exacerbated by the fact that our simulations of wave front healing through a forward scattering finite frequency kernel (which produces the 2ψ bias) may be less accurate than our

simulations of backward scattering (which produces the 1ψ bias) because the kernels may be too broad (e.g. Yoshizawa & Kennett 2002; Zhou *et al.* 2005) and multiple scattering is not modelled (Malcolm & Trampert 2011). It is reasonable to assume, however, that wave front healing, and therefore the 2ψ bias, would set on at about the period that the corresponding wavelength becomes comparable to the scale of major isotropic anomalies. By estimating this scale as ~ 200 km in the western United States, the 2ψ anisotropy is probably significantly biased only above about 50-s period, similar to 1ψ anisotropy. We present several lines of circumstantial evidence that point to the observed 40 s 2ψ map (Fig. 9c) being much less biased by isotropic structures than the maps above about 50-s period (Figs 8c and 9f).

First, the simulated 2ψ bias maps at 40 and 80 s shown in Figs 10(c) and (f) are very similar in the 2ψ fast directions and the distribution of high amplitude features, and differ mainly in the amplitude of the bias. However, the observed 40 and 80 s maps in Figs 9(c) and (f) are quite different from each other with a fast direction correlation coefficient equal only to 0.24 for regions where the amplitude of anisotropy is larger than 0.5 per cent. We believe this is because the observed 40 s map is dominated by intrinsic anisotropy whereas the 80 s map is much more strongly biased. It is unlikely that the intrinsic anisotropy at these two periods, which are both sensitive predominantly to the uppermost mantle, are uncorrelated. Second, close inspection reveals that the observed 40 and 80 s 2ψ

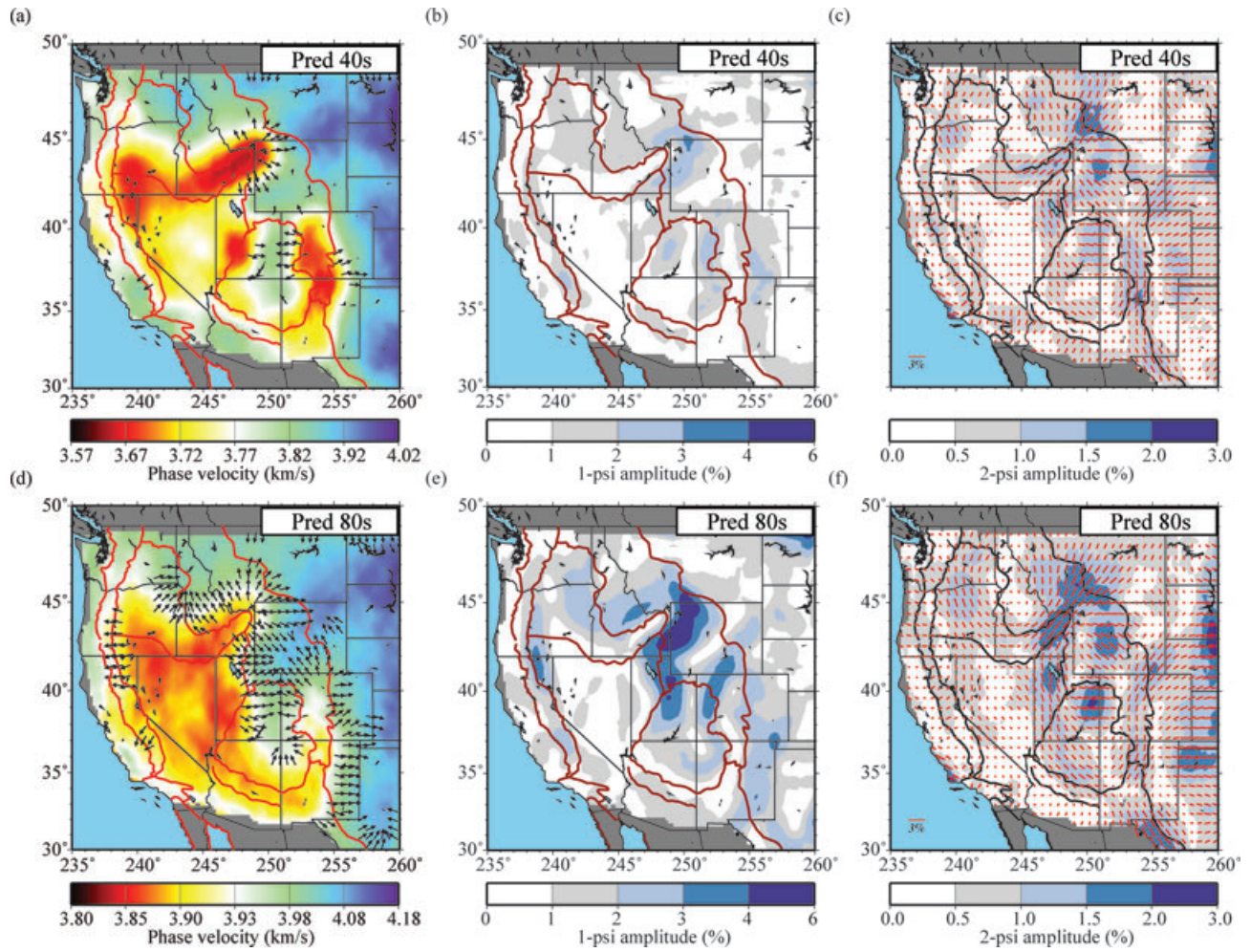


Figure 10. Same as Fig. 9, but with simulated measurements at 40 s (a)–(c) and 80 s (d)–(f) periods.

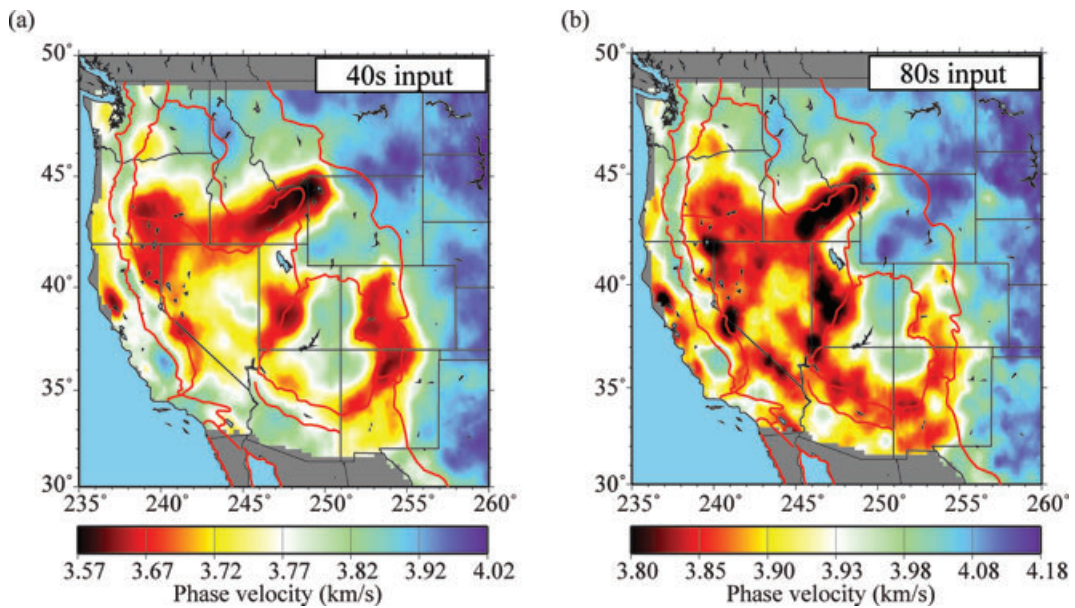


Figure 11. (a) The input model for the 40 s Rayleigh wave synthetic results shown in Figs 10(a)–(c). Panel (b) same as (a) but for the 80-s results shown in Figs 10(d)–(f).

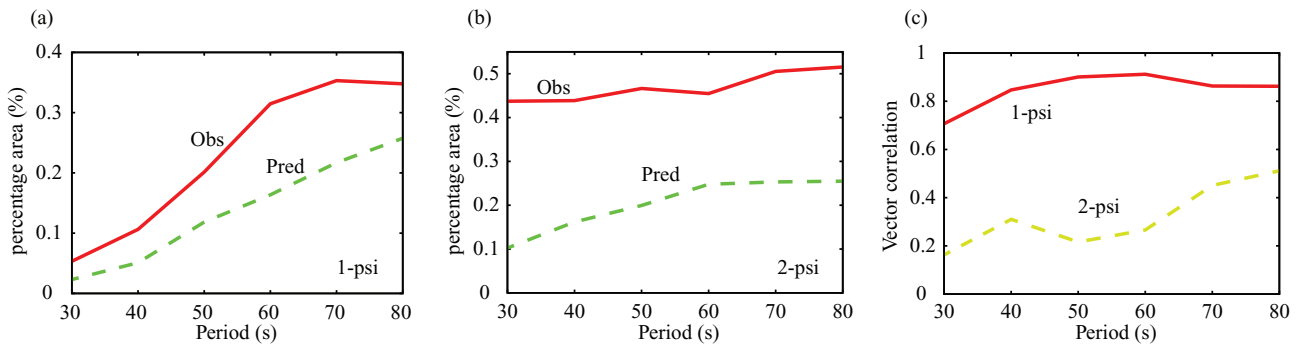


Figure 12. (a) Percentage of the studied region where the predicted (green dash line) or observed (solid red line) 1ψ anisotropy amplitude is greater than 2 per cent as a function of period. Panel (b) same as (a), but for 2ψ anisotropy greater than 1 per cent. (c) The correlation in the fast direction between the predicted and observed 1ψ (solid red line) and predicted and observed 2ψ (green dash line) anisotropy. Only regions with significant predicted anisotropy amplitudes (>2 per cent for 1ψ and >1 per cent for 2ψ) and meaningful observed anisotropy amplitudes (>1 per cent for 1ψ and >0.5 per cent for 2ψ) are included in the analysis.

maps differ mainly where the simulated 80 s 2ψ bias in Fig. 10(f) is largest. This suggests that our simulations correctly predict the location where the observed 2ψ anisotropy is likely to be biased at long periods. Third, as Fig. 12(b) shows, significant simulated 2ψ bias occurs at 40-s period over an area only about 1/3 the size of significant observed 2ψ anisotropy. Although we are concerned about the absolute accuracy of our 2ψ simulations, the relative area of significant 2ψ bias in our simulations more than doubles between 30- and 60-s period. Fourth, as Fig. 12(c) illustrates, at 70- and 80-s period the predicted and observed fast directions are better correlated ($\rho \sim 0.5$) with each other than at shorter periods, which implies that the isotropic bias in 2ψ anisotropy cannot be ignored at the longer periods.

This evidence is consistent with the belief that isotropic bias of 2ψ anisotropy is most severe above about 50-s period and the 2ψ maps based on ray theory (e.g. eikonal tomography) will be most reliable below this period. We acknowledge that this reasoning is not iron-clad, as our simulations have their limitations. Future efforts to improve the accuracy of the simulations of 2ψ bias would be useful. More useful, perhaps, would be efforts to model finite frequency effects in inversions directly, which is the approach taken by Lin & Ritzwoller (2011). This approach yields very different observed 2ψ anisotropy at 80-s period but very similar 2ψ anisotropy at 40-s period compared to the results presented here. In addition, the observed fast directions are better correlated across period. For example, the fast direction correlation coefficient between observations at 40- and 80-s period approximately doubles compared to the ray theoretic results presented here.

4.3 What are observers to do?

While the 1ψ and 2ψ isotropic bias are probably due to different finite frequency effects, as indicated by the synthetic tests (Fig. 4), the observation of a 1ψ component of anisotropy nevertheless should be considered as an indicator of some level of isotropic bias in the 2ψ component, particularly for regional applications. Although it is harder to discriminate the 2ψ isotropic bias from intrinsic anisotropy, the results shown in Section 4.2 suggest that the bias is probably important at periods >50 s where the 1ψ signal is particularly strong. Although the backward scattering should also affect traveltimes measurements near structure boundaries for global-scale tomography, the effect can be smeared out easily along long paths

and is probably less important. In fact, for any application, we believe that the isotropic 1ψ bias will only become important near a station when the dimension of the backward scattering sensitivity is approaching the resolution desired. Hence, the threshold for significant isotropic 1ψ bias may shift to longer periods for global tomography. However this is speculative and it would be prudent for global-scale modellers also to consider the recommendations here. In addition, surface wave dispersion measurements obtained from ambient noise are not exempt from isotropic bias. Ritzwoller *et al.* (2011) demonstrate that 1ψ anisotropy is also observed in ambient noise surface wave tomography at periods greater than ~ 50 s with the USArray.

First, observers would be well advised to estimate and report 1ψ anisotropy in their inversions. The observation of a weak 1ψ component of anisotropy is evidence for weak isotropic bias. A strong 1ψ signal is cause for concern that the 2ψ signal is biased and efforts must be taken to minimize the bias.

Second, observers are encouraged to model finite frequency effects, particularly wave front healing and backward scattering, in their inversion for azimuthal anisotropy. The use of finite frequency kernels that are not tuned to the measurements, however, may offer little help in reducing both the 1ψ and 2ψ bias. The weak correlation between the predicted and observed 2ψ fast directions where the predicted anisotropy amplitude is significant, as demonstrated in Fig. 12(c), is evidence that the ad-hoc finite frequency kernels used in this study may not faithfully reproduce the 2ψ bias effect. We note that we also carried out the synthetic experiments with oscillatory analytical kernels, which performed worse than the non-oscillatory kernels in matching the observed 1ψ bias. However, they produced geometrically similar results for the 2ψ bias but with reduced amplitudes. Lin & Ritzwoller (2011) discuss the effect of applying finite frequency corrections via the Helmholtz equation (eq. 2).

Third, the 1ψ signal may be misinterpreted as the 2ψ component of anisotropy when the data distribution is not homogeneous in azimuth. Fig. 13 presents examples using the directionally dependent phase velocity measurements shown in Fig. 7. The green line fits the observations in which both the 1ψ and 2ψ components are specified in the regression (i.e. eq. 3). The 2ψ part of this regression is shown with the black solid line. Thus, in Idaho near the Snake River Plain (Fig. 13b), simultaneous specification of the 1ψ and 2ψ components in the regression produces a 2ψ component with the small amplitude of 0.1 per cent. However, if the regression is

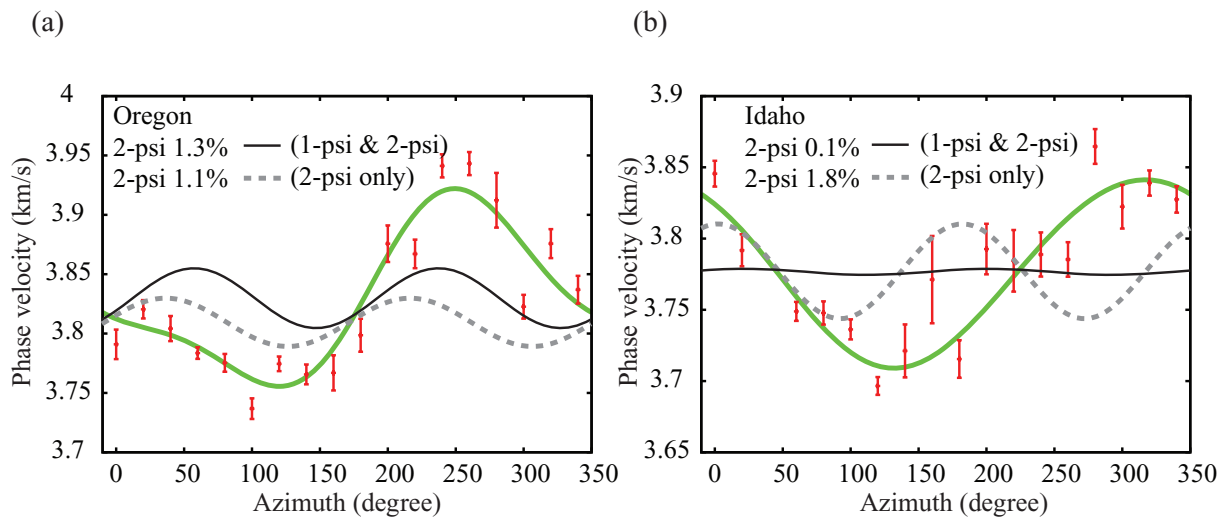


Figure 13. (a)–(b) Directionally dependent phase velocity measurements of 60 s Rayleigh wave obtained with the real data near the Snake River Plain and near the Cascade Range. (Same as Figs 7a and b but with two additional 2ψ curves.) The black thin line is the best-fitting 2ψ curve when both 1ψ and 2ψ are fit spontaneously and the dashed grey line is the best-fitting 2ψ curve when only the 2ψ component is fit. Both fast direction and amplitude can be quite different for the two 2ψ lines depending on if 1ψ is specified simultaneously in the regression.

performed without specifying the 1ψ component, then the 2ψ term attempts to fit the observed azimuthal distribution and the estimated amplitude of the 2ψ term increases to 1.8 per cent. The situation is not as severe near the Cascade Range in Oregon (Fig. 13a), but the 1ψ bias affects the orientation of the 2ψ fast direction by about 30° .

5 CONCLUSION

In this study, we discuss the significance of isotropic bias in measurements of azimuthally anisotropic phase velocities obtained from surface waves based on ray theoretic inversions. We demonstrate that significant 1ψ anisotropy bias, which is non-physical for surface wave velocity structure, is clearly observed in the western United States at long periods (>50 s) based on eikonal tomography (Lin *et al.* 2009) and USArray. The clear correlation between observed 1ψ anisotropy and sharp contrasts in isotropic structures and the fact that the amplitude of anisotropy increases with period strongly suggest that the 1ψ anisotropy is a form of isotropic bias caused by finite frequency effects that are unaccounted for in the inversion. This bias is probably also present in results based on other ray theoretic tomography methods particularly when the desired resolution is comparable to the dimension of the backward scattering sensitivity.

Most studies of finite frequency effects on surface waves have focused on wave front healing caused by forward scattering (e.g. Nolet & Dahlen 2000; Ritzwoller *et al.* 2002; Zhou *et al.* 2005; Malcolm & Trampert 2011). Near station finite frequency sensitivity, on the other hand, has rarely been explored, probably because the spatial extent of the region with strong backward scattering sensitivity is very small and it is surprising that its effect on long period surface wave measurements is important. Accurate expression of the near station sensitivity is particularly important for regional scale array studies such as our focus here (Yang & Forsyth 2006). Based on our simulations, the significant 1ψ signals that we observe near strong velocity contrasts as well as the spatial shift of the observed anomalies (e.g. Fig 6c) cannot be accounted for with the forward scattering part of the sensitivity kernel alone. They are explained, however, by

near station backward scattering that provides sensitivity that leads the arrival of the theoretical ray. Thought of ray theoretically, the back scattering part of the sensitivity kernel is caused by reflected signals propagating backward that interfere with the primary signal and affect the phase travelttime measurement. While surface waves reflected from sharp velocity contrasts have been identified at periods less than 30 s (e.g. Ji *et al.* 2005; Stich & Morelli 2007), the reflections discussed here merge with the main surface wave packet.

The effect of backward scattering on surface wave phase travelttime measurements is probably only strong when the distance between a sharp structural boundary and the station is within $\sim 3/16$ of wavelength. Considering the ~ 70 km station spacing for USArray, which is also roughly the dimension of the resolution for our tomography results (Lin *et al.* 2009), any structural boundary that appears right in the middle of two stations will cause no backward scattering effect when the wavelength is less than ~ 200 km, which roughly corresponds to 50 s Rayleigh wave. This is a plausible explanation for why finite frequency effects begin to manifest themselves at about 50-s period across the western United States in our results.

The observation of a 1ψ signal at long periods potentially provides a means to improve the resolution of structural boundaries at depth, which is crucial to distinguish thermal from composition structural variations in the upper mantle. To achieve this, however, precise knowledge of the near station sensitivity kernel will be required. Accurate expression of the sensitivity depends on the measurement method (Tromp *et al.* 2005). Here, we have chosen an exceptionally simple form for the finite frequency kernels and have found that the first-order patterns of the observed 1ψ signals are predicted relatively well. Although inferring a more accurate expression for the near station sensitivity is beyond the scope of this paper, we find that finite frequency kernels with near-station multiple side lobes do not predict the observed 1ψ anisotropy pattern. This may be because our measurement method is based on Frequency-Time Analysis (FTAN), which effectively removes the influence of wave groups that are well separated from the main arrival. A fully 3-D numerical simulation might be required to provide better insight (e.g. Fichtner *et al.* 2009; Tape *et al.* 2010).

Although estimating the 2ψ bias is not as straightforward as 1ψ bias due to the existence of intrinsic 2ψ azimuthal anisotropy, there are several lines of evidence that suggest the presence of 2ψ bias at long periods (>50 s) where the wavelength is comparable or larger than the scale of major isotropic structures in the region. Based on our synthetic tests, the 2ψ bias is mainly caused by wave front healing which arises from the broad forward scattering part of the sensitivity kernel, and correlation can be observed between predicted and observed 2ψ fast directions at long period (>60 s) where predicted 2ψ bias is strong. The strong isotropic bias in 2ψ anisotropy at long periods probably is responsible for the weak correlation between the observed 2ψ anisotropy fast directions across different periods. In a separate contribution, we show that the observed 2ψ anisotropy is better correlated across different periods when finite frequency effects are accounted for in the inversion (Lin & Ritzwoller 2011).

To evaluate isotropic bias in azimuthal anisotropy measurements properly, we encourage observers to estimate and report 1ψ anisotropy in their inversions, to model finite frequency effects using methods that are tailored to the method of measurement, and to estimate 1ψ and 2ψ anisotropy simultaneously.

ACKNOWLEDGMENTS

The authors thank the editor, Prof Jeannot Trampert, and an anonymous reviewer for constructive comments. Instruments (data) used in this study were made available through EarthScope (www.earthscope.org; EAR-0323309), supported by the National Science Foundation. The facilities of the IRIS Data Management System, and specifically the IRIS Data Management Center, were used for access the waveform and metadata required in this study. The IRIS DMS is funded through the National Science Foundation and specifically the GEO Directorate through the Instrumentation and Facilities Program of the National Science Foundation under Cooperative Agreement EAR-0552316. This work has been supported by NSF grants EAR-0711526 and EAR-0844097.

REFERENCES

Bensen, G.D., Ritzwoller, M.H., Barmin, M.P., Levshin, A.L., Lin, F., Moschetti, M.P., Shapiro, N.M. & Yang, Y., 2007. Processing seismic ambient noise data to obtain reliable broad-band surface wave dispersion measurements. *Geophys. J. Int.*, **169**(3), 1239–1260.

Bodin, T. & Maupin, V., 2008. Resolution potential of surface wave phase velocity measurements at small arrays. *Geophys. J. Int.*, **172**, 698–706, doi:10.1111/j.1365-246X.2007.03668.x

Chen, M. & Tromp, J., 2007. Theoretical and numerical investigations of global and regional seismic wave propagation in weakly anisotropic earth models. *Geophys. J. Int.*, **168**, 1130–1152, doi:10.1111/j.1365-246X.2006.03218.x

Fichtner, A., Kennett, B.L.N., Igel, H. & Bunge, H.-P., 2009. Full seismic waveform tomography for upper-mantle structure in the Australasian region using adjoint methods. *Geophys. J. Int.*, **179**, 1703–1725, doi:10.1111/j.1365-246X.2009.04368.x

Friederich, W., Hunzinger, S. & Wielandt, E., 2000. A note on the interpretation of seismic surface waves over three-dimensional structures. *Geophys. J. Int.*, **143**, 335–339.

Ji, C., Tsuboi, S., Komatitsch, D. & Tromp, J., 2005. Rayleigh-wave multipathing along the West coast of North America. *Bull. seism. Soc. Am.*, **95**, 2115–2124.

Lin, F., Moschetti, M.P. & Ritzwoller, M.H., 2008. Surface wave tomography of the western United States from ambient seismic noise: Rayleigh and Love wave phase velocity maps. *Geophys. J. Int.*, **173**(1), 281–298.

Lin, F., Ritzwoller, M.H. & Snieder, R., 2009. Eikonal tomography: surface wave tomography by phase front tracking across a regional broad-band seismic array. *Geophys. J. Int.*, **177**(3), 1091–1110.

Lin, F.-C. & Ritzwoller, M.H., 2010. Empirically determined finite frequency sensitivity kernels for surface waves. *Geophys. J. Int.*, **182**, 923–932, doi:10.1111/j.1365-246X.2010.04643.x

Lin, F.C. & Ritzwoller M.H., 2011. Helmholtz surface wave tomography for isotropic and azimuthally anisotropic structure. *Geophys. J. Int.*, in press, doi:10.1111/j.1365-246X.2011.05070.x

Lin, F.C., Ritzwoller, M.H., Yang, Y., Moschetti, M.P., & Fouch, M.J., 2011. Complex and variable crustal and uppermost mantle seismic anisotropy in the western United States. *Nat. Geosci.*, **4**, 55–61, doi:10.1038/ngeo1036.

Malcolm, A.E. & Trampert, J., 2011. Tomographic errors from wave front healing: more than just a fast bias. *Geophys. J. Int.*, **185**, 385–402, doi:10.1111/j.1365-246X.2011.04945.x

Marone, F. & Romanowicz, B., 2007. The depth distribution of azimuthal anisotropy in the continental upper mantle. *Nature*, **447**, 198–201.

Moschetti, M.P., Ritzwoller, M.H., Lin, F. & Yang, Y., 2010a. Seismic evidence for widespread western-US deep-crustal deformation caused by extension. *Nature*, **464**, 885–889.

Moschetti, M.P., Ritzwoller, M.H., Lin, F. & Yang, Y., 2010b. Crustal shear wave velocity structure of the western United States inferred from ambient seismic noise and earthquake data. *J. geophys. Res.*, **115**, B10306, doi:10.1029/2010JB007448.

Nolet, G. & Dahlen, F.A., 2000. Wave front healing and the evolution of seismic delay times. *J. geophys. Res.*, **105**(B8), 19 043–19 054, doi:10.1029/2000JB900161.

Peter, D., Tape, C., Boschi, L. & Woodhouse, J.H., 2007. Surface wave tomography: global membrane waves and adjoint methods. *Geophys. J. Int.*, **171**, 1098–1117.

Pollitz, F.F. & Snoko, J.A., 2010. Rayleigh-wave phase-velocity maps and three-dimensional shear velocity structure of the western US from local non-plane surface wave tomography. *Geophys. J. Int.*, **180**, 1153–1169.

Ritzwoller, M.H., Lin, F. & Shen, W., 2011. Ambient noise tomography with a large continental seismic array. *Compte Rendus Geoscience*, in press, doi:10.1016/j.crte.2011.03.007.

Ritzwoller, M.H., Shapiro, N.M., Barmin, M.P. & Levshin, A.L., 2002. Global surface wave diffraction tomography. *J. geophys. Res.*, **107**, B12, doi:10.1029/2002JB001777.

Sieminski, A., Liu, Q., Trampert, J. & Tromp, J., 2007. Finite-frequency sensitivity of surface waves to anisotropy based upon adjoint methods. *Geophys. J. Int.*, **168**, 1153–1174, doi:10.1111/j.1365-246X.2006.03261.x

Sieminski, A., Trampert, J. & Tromp, J., 2009. Principal component analysis of anisotropic finite-frequency sensitivity kernels. *Geophys. J. Int.*, **179**, 1186–1198, doi:10.1111/j.1365-246X.2009.04341.x

Smith, M.L. & Dahlen, F.A., 1973. Azimuthal dependence of Love and Rayleigh-wave propagation in a slightly anisotropic medium. *J. geophys. Res.*, **78**, 3321–3333.

Smith, W.H.F. & Wessel, P., 1990. Gridding with continuous curvature splines in tension. *Geophysics*, **55**, 293–305.

Snieder, R., 3D Linearized scattering of surface waves and a formalism for surface wave holography. *Geophys. J. R. astr. Soc.*, **84**, 581–605, 1986.

Stich, D. & Morelli, A., 2007. Reflection of seismic surface waves at the northern Apennines. *Earth planet. Sci. Lett.*, **259**, 149–158.

Tape, C., Liu, Q., Maggi, A. & Tromp, J., 2010. Seismic tomography of the southern California crust based on spectral-element and adjoint methods. *Geophys. J. Int.*, **180**, 433–462.

Tromp, J., Tape, C. & Liu, Q., 2005. Seismic tomography, adjoint methods, time reversal and banana-doughnut kernels. *Geophys. J. Int.*, **160**, 195–216, doi:10.1111/j.1365-246X.2004.02453.x

Wielandt, E., 1993. Propagation and structural interpretation of non-plane waves. *Geophys. J. Int.*, **113**, 45–53.

Yang, Y. & Forsyth, D.W., 2006. Regional tomographic inversion of amplitude and phase of Rayleigh waves with 2-D sensitivity kernels. *Geophys. J. Int.*, **166**, 1148–1160.

- Yang, Y., Ritzwoller, M.H., Lin, F.-C., Moschetti, M.P. & Shapiro, N.M., 2009. The structure of the crust and uppermost mantle beneath the western US revealed by ambient noise and earthquake tomography, *J. geophys. Res.*, **113**, B12310, doi:10.1029/2008JB005833.
- Yoshizawa, K. & Kennett, B.L.N., 2002. Determination of the influence zone for surface wave paths. *Geophys. J. Int.*, **149**, 441–454.
- Zhou, Y., Dahlen, F.A. & Nolet, G., 2004. Three-dimensional sensitivity kernels for surface wave observables. *Geophys. J. Int.*, **158**, 142–168.
- Zhou, Y., Dahlen, F.A., Nolet, G. & Laske, G., 2005. Finite-frequency effects in global surface-wave tomography, *Geophys. J. Int.*, **163**, 1087–1111.